JOURNAL OF APPLIED PHYSICS **117**, 155103 (2015)

Suppressing the bipolar contribution to the thermoelectric properties of $Mg_2Si_{0.4}Sn_{0.6}$ by Ge substitution

Libin Zhang,[1,a)] Penghao Xiao,[2] Li Shi,[1,3] Graeme Henkelman,[2] John B. Goodenough,[1,3] and Jianshi Zhou[1,3]
[1]*Materials Science and Engineering Program, University of Texas at Austin, Austin, Texas 78712, USA*
[2]*Department of Chemistry and the Institute for Computational and Engineering Sciences, University of Texas at Austin, Austin, Texas 78712, USA*
[3]*Department of Mechanical Engineering, The University of Texas at Austin, Austin, Texas 78712, USA*

(Received 16 January 2015; accepted 4 April 2015; published online 20 April 2015)

The optimized thermoelectric figure of merit (ZT) of $Mg_2Si_{0.4}Sn_{0.6}$ peaks at about 750 K because its relatively narrow band gap results in pronounced bipolar transport at higher temperatures. To suppress the bipolar transport, we have conducted a combined experimental and theoretical investigation of Ge-substitution effects on the band structures and thermoelectric properties of Sb-doped $Mg_2Si_{0.4}Sn_{0.6-y}Ge_y$ ($y = 0$, 0.1, and 0.2) synthesized by solid state reaction. The measured transport properties of these compositions can be interpreted by a triple-parabolic-band model based on first-principle calculation of band structures. The results show that the bipolar conduction in the temperature range up to 800 K was effectively suppressed by Ge substitution that widens the band gap. As a side effect, Ge substitution induces the separation of two otherwise converged conduction bands in $Mg_2Si_{0.4}Sn_{0.6}$, leading to reduced thermoelectric performance at low temperatures. The result of these two competing effects is that Ge-substituted samples achieve the maximum power factor similar to that of $Mg_2Si_{0.4}Sn_{0.6}$, but with an increased peak temperature. In addition, Ge substitution reduces the bipolar thermal conductivity while maintaining the low lattice thermal conductivity of $Mg_2Si_{0.4}Sn_{0.6}$. © *2015 AIP Publishing LLC*.
[http://dx.doi.org/10.1063/1.4918311]

I. INTRODUCTION

Thermoelectric (TE) devices have received renewed research interest because of potential applications in waste heat recovery and refrigeration. The heat to electric power conversion efficiency of such devices is characterized by the dimensionless figure of merit (ZT) of the constituent thermoelectric materials. ZT is calculated as $ZT = \frac{S^2\sigma}{\kappa_L+\kappa_e}T$, where S is the Seebeck coefficient, σ is the electrical conductivity, T is the absolute temperature, κ_L and κ_e are the lattice and electronic contributions to the thermal conductivity, respectively. S, σ, and κ_e are correlated electronic properties, while κ_L depends on crystal structure and chemical bonding. In order to improve ZT, a variety of approaches have been explored to enhance the power factor $S^2\sigma$ and reduce κ_L. It has been reported that increasing conducting band degeneracy could effectively enhance the Seebeck coefficient without sacrificing the electrical conductivity.[1] It has also been demonstrated that some chemical doping can introduce additional resonant electronic states and increase the total electronic density of states near the Fermi energy, so that the power factor increases.[2] On the other hand, the approaches for reducing κ_L include employing crystal structures with pronounced anharmonicity in the atomic bonding,[3] complex crystal structures,[4–6] alloying,[7] and nanostructuring,[8,9] which enhance phonon scattering by phonons, defects, or grain boundaries.

Electron-doped $Mg_2Si_xSn_{1-x}$ solid solutions are promising n-type TE materials for waste heat recovery because of their high thermoelectric performance as well as the low cost, earth abundance, and environmental friendliness of the majority of the constituent elements. $Mg_2Si_xSn_{1-x}$ crystallizes in the anti-fluorite crystal structure with the space group $Fm\bar{3}m$, as shown in the schematic drawing of Fig. 1(a). With such a simple crystal structure, the lattice thermal conductivities of $Mg_2Si_xSn_{1-x}$ solid solutions are as low as 2.0 W m^{-1} K^{-1} owing to a large mass mismatch between Si and Sn.[10] Besides the low lattice thermal conductivity, Zaitsev *et al.* suggested that two conduction bands converge at an optimized composition in $Mg_2Si_xSn_{1-x}$, $x = 0.6$, giving rise to a high band degeneracy and therefore an enhanced ZT.[10] Liu *et al.* later systematically investigated the thermoelectric properties of $Mg_2Si_xSn_{1-x}$ series from $x = 0.2$ to $x = 0.8$ and concluded that the $x = 0.7$ sample gives the highest ZT, in agreement with their density functional theory (DFT) calculation that predicted two conduction bands converge at $x = 0.7$.[11]

However, the $Mg_2Si_xSn_{1-x}$ sample with a higher Sn content, $x = 0.6$ to 0.7, has a relatively narrow band gap owing to the small band gap of Mg_2Sn.[12] In a narrow band-gap semiconductor, intrinsic carriers can be thermally excited, leading to the co-existence of electron and hole transport.[13] Such bipolar transport decreases the Seebeck coefficient because of the opposite signs that electron and hole contribute to the Seebeck coefficient. It also results in an additional contribution to the thermal conductivity due to

a)libinzhang@utexas.edu

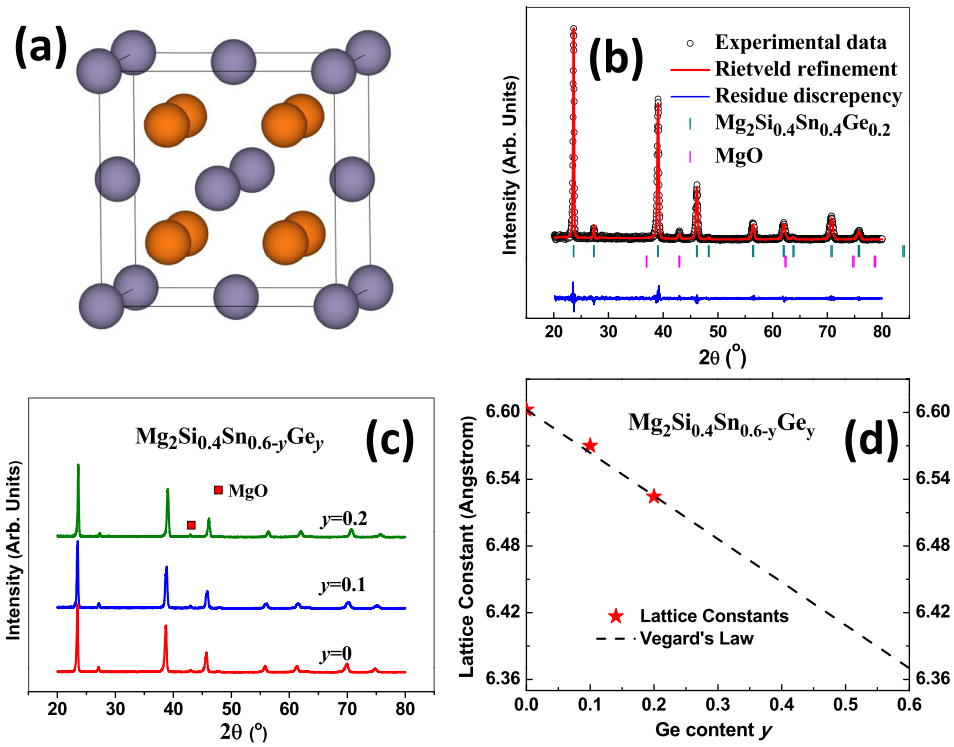

FIG. 1. (a) The crystal structure of $Mg_2(Si,Ge,Sn)$ (color key: yellow-Mg and grey-Si/Ge/Sn); (b) XRD pattern of $Mg_2Si_{0.4}Sn_{0.4}Ge_{0.2}$ together with the results of the Rietveld refinement; (c) the XRD patterns of $Mg_2Si_{0.4}Sn_{0.6-y}Ge_y$ ($y = 0$, 0.1, and 0.2) samples doped with Sb; (d) the change of lattice parameters with increasing Ge substitution in $Mg_2Si_{0.4}Sn_{0.6-y}Ge_y$. The lattice parameter shown for $Mg_2Si_{0.4}Ge_{0.6}$ is the value given in Ref. 12.

the presence of both electron and hole currents that carry non-zero Peltier heat even under zero net electrical current condition.[14] Consequently, the bipolar effect decreases the *ZT* at temperatures where the intrinsic thermal excitation is significant. For example, Bi_2Te_3 and PbTe, the state-of-the-art TE materials, show *ZT* peaks at relative low temperatures; their ZT value are reduced at high temperatures due to their narrow band gaps and therefore the bipolar effect.[15] Similarly, the peak *ZT* of $Mg_2Si_xSn_{1-x}$ occurs at the temperature near 750 K,[10] above which the bipolar effects results in a decreased *ZT*. Increasing the band gap could possibly improve the *ZT* at high temperatures by preventing the bipolar transport effect.[16]

Here, we report an investigation of Ge substitution of Sn to increase the band gap of $Mg_2Si_{0.4}Sn_{0.6}$ so as to suppress the bipolar effect. This investigation is motivated by prior reports that Mg_2Ge has a larger band gap (0.74 eV) than that in Mg_2Sn (0.35 eV).[12] Moreover, when compared to Mg_2Si that has a similar band gap of 0.78 eV, the band gap of Mg_2Ge decreases relatively slowly with increasing temperature. Specifically, the temperature dependence of band gap in Mg_2Ge is -1.8×10^{-4} eV/K while that of Mg_2Si is -6×10^{-4} eV/K.[12] In addition, introducing Ge into $Mg_2Si_xSn_{1-x}$ may increase the complexity of band structure[17] as well as the structure disorder that may further reduce the lattice thermal conductivity.[18,19]

In Secs. II and III, we first report the measured TE properties of Sb-doped $Mg_2Si_{0.4}Sn_{0.6-y}Ge_y$ ($y = 0$, 0.1, and 0.2) samples prepared by the solid-state reaction and consolidated by spark plasma sintering (SPS). Then, we investigate the band structures by DFT calculation in conjunction with Vegard's law. Finally, a triple-parabolic-band (TPB) model is developed to quantitatively understand the relationship between TE properties and band structures in $Mg_2Si_{0.4}Sn_{0.6-y}Ge_y$ solid solutions. Based on this TPB model, we also calculate the bipolar thermal conductivity and extract the lattice thermal conductivity.

II. EXPERIMENTAL METHODS

A. Materials preparation

We synthesized Sb-doped $Mg_2Si_{0.4}Sn_{0.6-y}Ge_y$ ($y = 0$, 0.1, and 0.2) solid solutions with a one-step solid state reaction method that was carried out in a reductive environment. The stoichiometric amounts of Mg (99.8%, 325 mesh), Si (99.999%, 325 mesh), Sn (99.8%, 325 mesh), Ge (99.999%, 100 mesh), and Sb (99.5%, 325 mesh) powder, with an extra 15–17 mol. % of Mg[20] were well mixed in an agate mortar. Sb at 0.5–1.5 mol. % was doped on the Si/Sn/Ge site to achieve the different carrier concentration. This powder mixture was then pressed into pellets under 20 MPa pressure. Afterwards, the pellets were wrapped in a Mo foil before being placed in the center of a tube furnace with a flow of mixture gas of Ar and H_2 in ratio of 95:5. These samples were sintered for 15 h at 1023 K. After the sintering was completed, the products were taken out of the furnace, ground into fine powders, and consolidated into hard pellets by using the SPS method at 1023–1073 K under 50 MPa for 8 min. The final products show densities over 98% of the theoretical value. The gain size of the resulting product is typically serval microns, which is comparable to those samples prepared in a similar manner.[21,22]

B. Characterizations and measurements

The phase purity and the crystal structure of samples were characterized by X-ray diffraction (XRD) on a Phillip X'pert diffractometer with Cu Kα radiation. The pellets were cut into 6 mm × 6 mm × 1 mm squares for Hall coefficient, Seebeck coefficient, electrical conductivity, and thermal

diffusivity measurements. The electrical conductivity was measured with a Physical Properties Measurement System (PPMS, Quantum Design) by using the van der Pauw method in the temperature range from 2 K to 300 K, and by using the four-probe method with a homemade setup from 300 K to 800 K. The Seebeck coefficients were measured on two homemade setups within the temperature ranges from 80 K to 300 K and 300 K to 800 K. The Hall coefficients at 300 K were measured on the PPMS. The thermal diffusivity (D) was measured by using the laser flash method on a Netzsch LFA 457 apparatus. In order to protect the sample from oxidation from residue oxygen during the measurements, a 20-nanometer thick Al_2O_3 layer was coated on the sample surface.[30] The heat capacity (C_p) was measured with the PPMS in the temperature range from 2 K to 380 K. It is worth noting that the C_p values measured at 380 K are slightly higher than the theoretical value calculated by Dulong-Petit law. Thus, we adopted the C_p value measured at 380 K for higher temperatures. Thermal conductivity is calculated from the equation $\kappa = D \times \rho \times C_p$. The density of samples ρ was measured by using the Archimedes' method.

III. RESULTS AND ANALYSIS

A. Materials characterization

The XRD patterns of the as-synthesized $Mg_2Si_{0.4}Sn_{0.6-y}Ge_y$ ($y = 0$, 0.1, and 0.2) samples can be refined in the anti-CaF_2 crystal structure, as shown in Figs. 1(b) and 1(c). The lattice parameters of the $Mg_2Si_{0.4}Sn_{0.6-y}Ge_y$ ($y = 0$, 0.1, and 0.2) solid solutions are obtained from the Rietveld refinement of XRD patterns (listed in Table I). As presented in Fig. 1(d), the lattice parameters reduced linearly with the Ge content y, following Vegard's law, which indicates that Ge atoms successfully substitute for Sn. A small peak at $2\theta \approx 43^\circ$ corresponds to a MgO impurity phase of around 8 wt. % in all samples (details shown in Table I). The MgO phase is almost unavoidable, since Mg is volatile and highly reactive to residue oxygen at high temperatures. In our method, the reductive Ar/H_2 gas effectively suppressed the oxygen partial pressure during sintering. Since the MgO impurity content presents in all three samples is nearly identical, we believe that the systematic changes in the TE properties of $Mg_2Si_{0.4}Sn_{0.6-y}Ge_y$ ($y = 0$, 0.1, and 0.2) are primarily caused by Ge substitutions.

B. Thermoelectric properties

Fig. 2 shows the temperature-dependent thermoelectric properties of $Mg_2(Si_{0.4}Sn_{0.6-y}Ge_y)_{0.99}Sb_{0.01}$ with Hall coefficients (R_H) of $2.4(\pm 0.2) \times 10^{-8} m^3\ C^{-1}$ measured at room temperature. As shown in Fig. 2(a), the Seebeck coefficient (S) of $Mg_2Si_{0.4}Sn_{0.6-y}Ge_y$ samples are all negative corresponding to n-type doping. For $Mg_2Si_{0.4}Sn_{0.6}$, the rise of S value with temperature is suppressed at temperatures above 650 K. This behavior indicates the onset of intrinsic carrier excitation and bipolar transport. Such bipolar suppression of Seebeck coefficient in $Mg_2Si_{0.4}Sn_{0.6}$ is also evident in previously reported experimental data, especially in the samples with low carrier concentrations.[10,23,24] In contrast, for $Mg_2Si_{0.4}Sn_{0.4}Ge_{0.2}$, S increases nearly linearly with temperature up to 800 K. Overall, for samples with the same Sb doping concentration and similar Hall coefficient, increasing Ge substitution y in $Mg_2Si_{0.4}Sn_{0.6-y}Ge_y$ ($y = 0$, 0.1, and 0.2) lowers the absolute value of S before the onset temperature of bipolar conduction. When temperature continues to rise, however, the Seebeck coefficients of Ge-substituted samples become comparable to that of $Mg_2Si_{0.4}Sn_{0.6}$, as a result of elimination of the bipolar effect.

The suppression of bipolar effects in Ge-substituted samples is also evident in the thermal conductivity results shown in Fig. 2(b). The κ of $Mg_2Si_{0.4}Sn_{0.6}$ decreases with temperature until it reaches a minimum at 650 K, above which the bipolar transport starts to contribute significantly to the total thermal conductivity. In contrast, although the κ value of the Ge-substituted samples are higher than that $Mg_2Si_{0.4}Sn_{0.6}$ at low temperatures, they monotonically decrease with temperature until 800 K. Specifically, the κ of the intermediate composition, $Mg_2Si_{0.4}Sn_{0.5}Ge_{0.1}$, becomes lowest among the three samples at temperatures above 700 K, although the difference is comparable to the measurement uncertainty.

Fig. 2(c) shows that the electrical conductivities of all three Sb-doped $Mg_2Si_{0.4}Sn_{0.6-y}Ge_y$ samples decrease with increasing temperature. The electrical conductivity increases with increasing Ge content y, while the difference decreases with increasing temperature. The calculated dimensionless ZT are presented in Fig. 2(d). It is noted that the propagated relative uncertainty of ZT values calculated from the three measured properties is as much as about 13%, making it difficult to clearly identify the ZT difference among the three samples. Nevertheless, at temperature below 650 K, the ZT of $Mg_2Si_{0.4}Sn_{0.6}$ appears to be the highest among three samples. However, the ZT for this sample peaks at $T_{max} \approx 750$ K. The ZT decreases as temperature further increases because of the onset of bipolar effect. In contrast, the ZT keeps increasing at high temperatures $T > 650$ K for the Ge substituted samples. It appears that T_{max} for the Ge-substituted samples moves to a higher temperature: the higher the Ge concentration, the higher T_{max}. Within the measured temperature

TABLE I. The crystal structure and phase information of $Mg_2Si_{0.4}Sn_{0.6-y}Ge_y$ ($y = 0$, 0.1, and 0.2) obtained from the Rietveld refinement of the XRD patterns. Bragg R-factor and χ^2 stand for Rietveld reliability factor and goodness of fit, respectively.

Ge composition y	Lattice parameter (Å)	Cell volume (Å^3)	Theoretical density (g/cm^3)	Measured density (g/cm^3)	MgO (wt. %)	Bragg R-factor	χ^2
0	6.6024	287.81	3.03	3.01	7.43	2.73	0.95
0.1	6.5701	283.60	2.97	2.94	8.11	3.92	0.85
0.2	6.5244	277.73	2.93	2.92	8.49	3.66	0.92

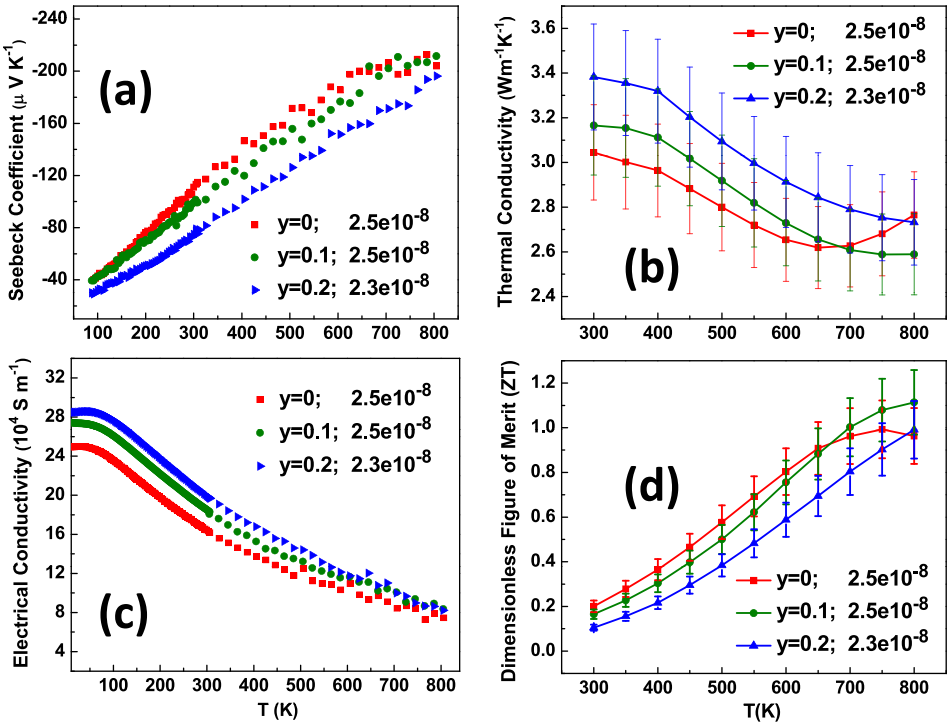

FIG. 2. Temperature-dependent (a) Seebeck coefficient with 5% uncertainty, (b) thermal conductivity with 7% uncertainty, (c) electrical conductivity with 5% uncertainty, and (d) dimensionless *ZT* of Sb-doped $Mg_2Si_{0.4}Sn_{0.6-y}Ge_y$ ($y = 0$, 0.1, and 0.2) with 13% uncertainty. All these samples show the approximately the same Hall coefficient of 2.4 $(\pm 0.2) \times 10^{-8}$ m^3 C^{-1}. Each sample is labeled with Ge substitution level y and Hall coefficient with the unit of m^3 C^{-1}.

range, the maximum *ZT*, 1.1, among the three samples is achieved in $Mg_2Si_{0.4}Sn_{0.5}$ $Ge_{0.1}$ at 800 K.

C. Electronic band structure

In order to understand the underlying relationship between the chemical composition and band structure in $Mg_2Si_{0.4}Sn_{0.6-y}Ge_y$, we obtained the band structures of two end-point compositions, i.e., $Mg_2Si_{0.375}Sn_{0.625}$ and $Mg_2Si_{0.375}Ge_{0.625}$, by DFT calculation. The PBE functional was used to account for the exchange correlation energy during geometry optimizations, and then the hybrid functional, HSE06 form,[25–27] was employed for the band structure calculations. All the calculations were performed in the Vienna *Ab-initio* simulation package (VASP). Valence electrons were expanded in a plane wave basis set[28,29] with an energy cutoff of 246 eV, and core electrons were described by the projector augmented wave (PAW) method. A supercell composed of $2 \times 2 \times 2$ unit cells was constructed, in which there were 8 equivalent positions of Si/Sn/Ge. The PBE functional significantly underestimates band gaps due to the electron self-repulsion error and predicts all the compounds to be metal. The hybrid HSE06 gives rise to more accurate band gap results, although it may still not exactly reproduce experimental values. The trend of band gap change upon alloying can be captured by HSE06.

Figs. 3(a) and 3(b) show the calculated band structures of $Mg_2Si_{0.375}Sn_{0.625}$ and $Mg_2Si_{0.375}Ge_{0.625}$. It is known that Mg_2(Si, Sn, and Ge) solid solutions are indirect-band-gap semiconductors, as illustrated schematically in Fig. 4(a). The band structures presented in Figs. 3(a) and 3(b) look rather like semiconductors with direct band gap because of the zone folding of the $2 \times 2 \times 2$ supercell used in this calculation. Fig. 3(c) presents the zone-folding effect in the first Brillouin zone of a Mg_2X (X = Si, Sn, or Ge) primitive cell. It has been reported that two conduction band bottoms locate on X point and valance band tops locate on Γ point in the primitive cell representation.[10,30] In the $2 \times 2 \times 2$ supercell representation, the original X points (marked as black in Fig. 3(c)) are folded to the Γ point. The center-points of Γ-X lines becomes the new X points (marked as red). In Figs. 3(a) and 3(b), at the Γ point, the two conduction bands in blue and green are folded here from the original X point along the k_y axis when the original Γ-X line shrinks by half. Those extra magenta bands are folded from the original equivalent X points along the k_x and k_z axes. The three directions (k_x, k_y, and k_z) should be isotropic for a perfectly random alloy and thus one band folded along these three directions should be degenerate at the Γ point. However, in this calculation, the supercell is too small to yield the alloy randomness. This artificial asymmetry causes energy splitting of the equivalent bands at the Γ point. Despite this discrepancy, it is clear in Fig. 3 that the band gap of 0.59 eV for $Mg_2Si_{0.375}Ge_{0.625}$ is significantly larger than that of 0.28 eV for $Mg_2Si_{0.375}Sn_{0.625}$. The two conduction bands (green and blue) in $Mg_2Si_{0.375}Sn_{0.625}$ are almost converged while they are separated by approximately 0.31 eV in $Mg_2Si_{0.375}Ge_{0.625}$. Linear extrapolation of the band structures from these two endpoints, following Vegard's law, suggests that as Ge content y increases by 0.1, both E_g and dE increase approximately by 0.05 eV in $Mg_2Si_{0.4}Sn_{0.6-y}Ge_y$. It is worth-noting that no significant change in band curvatures was observed between $Mg_2Si_{0.375}Sn_{0.625}$ and $Mg_2Si_{0.375}Ge_{0.625}$. Overall, this DFT calculation suggests that Ge substitution has similar effects on changing band structures as increasing Si content in $Mg_2Si_xSn_{1-x}$, in terms of changing the band gap and conduction-band splitting. However, as we discussed earlier, the negative temperature dependence of band gap in Mg_2Ge is much smaller than that in Mg_2Si. Ge substitution is thus

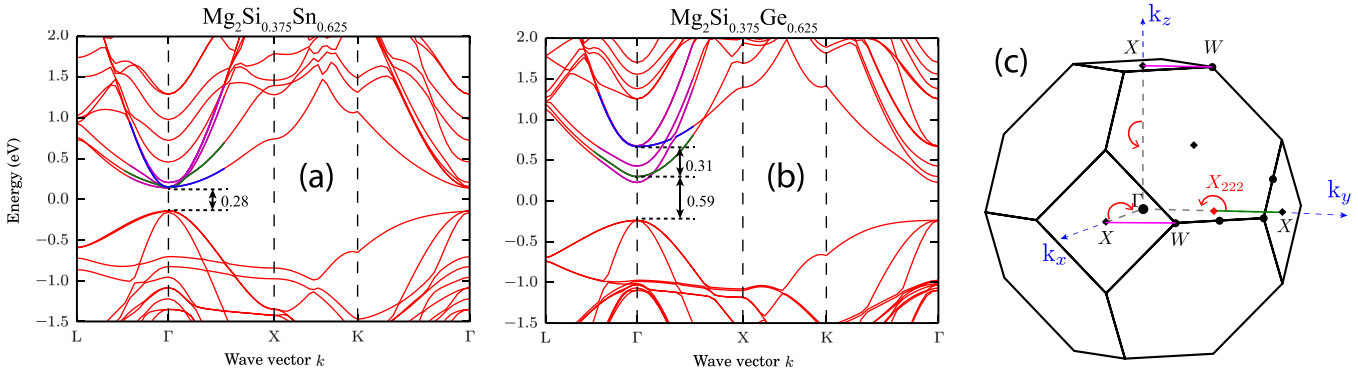

FIG. 3. The electronic band structures of (a) $Mg_2Si_{0.375}Sn_{0.625}$ and (b) $Mg_2Si_{0.375}Ge_{0.625}$ obtained by DFT calculation. The blue and green bands represent the two bands folded from the original X points along the Γ–*X* line in k_y direction in the primitive cell representation; the magenta bands near the conduction band bottom are folded from the original X points at k_x and k_z directions in the primitive cell representation. (c) Zone-folding effect represented in the first Brillouin zone upon the use of $2 \times 2 \times 2$ supercell.

more appealing for the purpose of widening band gap at high temperatures.

D. Triple-parabolic-band modeling and analysis

The band-gap widening and conduction-band separation induced simultaneously by Ge substitution have competing effects on the TE properties. The increased E_g is expected to suppress the bipolar effects and improve *ZT* at high temperatures. However, an increased *dE* can reduce band degeneracy and thus reduce *ZT*. We have developed a TPB model to quantify these two effects on the TE properties of $Mg_2Si_{0.4}Sn_{0.6-y}Ge_y$. The model considers two conduction bands, namely, the light conduction band 1 and the heavy conduction band 2, and one valence band 3, which are shown in Fig. 4(a). Based on this TPB model, we derived equations of Seebeck coefficient (S), electrical conductivity (σ), and Hall coefficient (R_H) by following the classic two-band model. The detailed derivation procedure is presented in Appendix A. The equations are listed as follows:

$$S = \frac{S_1\sigma_1 + S_2\sigma_2 + S_3\sigma_3}{\sigma_1 + \sigma_2 + \sigma_3}, \tag{1}$$

$$\sigma = \sigma_1 + \sigma_2 + \sigma_3, \tag{2}$$

and

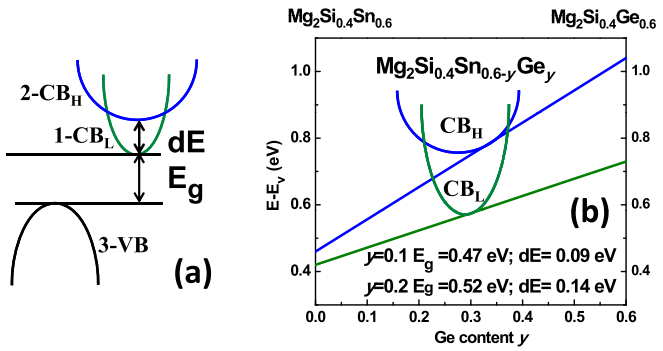

FIG. 4. (a) Schematically illustrated electronic band structures of $Mg_2Si_{0.4}Sn_{0.6-y}Ge_y$ in a primitive cell representation, where the blue curve indicates the heavy conduction band (CB_H) and the green curve indicates the light conduction band (CB_L); and (b) Ge composition-dependent conduction band energies relative to the valence band.

$$R_H = \frac{R_{H,1}\sigma_1^2 + R_{H,2}\sigma_2^2 + R_{H,3}\sigma_3^2}{(\sigma_1 + \sigma_2 + \sigma_3)^2}. \tag{3}$$

Here, S_i, σ_i, and $R_{H,i}$ stand for the partial Seebeck coefficient, electrical conductivity, and Hall coefficient of band i with $i = 1$, 2, and 3, respectively. The detailed equations of S_i, σ_i, and $R_{H,i}$ can be found in Appendix B.

A self-consistent band gap $E_g = 0.42$ eV of $Mg_2Si_{0.4}Sn_{0.6}$ was obtained by fitting the measured transport properties of two $Mg_2Si_{0.4}Sn_{0.6}$ samples with different Sb doping. The conduction bands separation (*dE*) of $Mg_2Si_{0.4}Sn_{0.6}$, 0.04 eV is adopted from the literature.[30–32] All the modeling parameters of $Mg_2Si_{0.4}Sn_{0.6}$, both fitted and adopted from the literature, are listed in Appendix C, Table II. Subsequently, as shown in Fig. 4(b), the E_g and *dE* values for Ge-substituted samples are estimated based on those of $Mg_2Si_{0.4}Sn_{0.6}$ and the linear extrapolation of DFT results: $E_g = 0.47$ eV; $dE = 0.09$ eV for $Mg_2Si_{0.4}Sn_{0.5}Ge_{0.1}$ and $E_g = 0.52$ eV; $dE = 0.14$ eV for $Mg_2Si_{0.4}Sn_{0.4}Ge_{0.2}$. By only replacing the band gap (E_g) and conduction-band separation (*dE*) in the TPB model, we then calculated the transport properties of $Mg_2Si_{0.4}Sn_{0.5}Ge_{0.1}$ and $Mg_2Si_{0.4}Sn_{0.4}Ge_{0.2}$. The detailed fitting and calculation procedures are presented in Appendixes C and D. Fig. 5(a) displays the modeling results together with the experimental data of power factor (*PF*) for $Mg_2Si_{0.4}Sn_{0.6-y}Ge_y$ ($y = 0$, 0.1, and 0.2) with the Hall coefficients of $2.4(\pm 0.2) \times 10^{-8}$ m^3 C^{-1}. A good match between the experimental results and calculation curves indicates that the increase of E_g and *dE* is primarily responsible for the changes of TE properties in $Mg_2Si_{0.4}Sn_{0.6-y}Ge_y$ ($y = 0.1$ and 0.2).

As mentioned earlier, the conduction-band separation and band-gap widening have competing effects on TE properties. In order to demonstrate these two effects, we have calculated the power factor of a hypothetical material with an increased band gap ($E_g = 0.52$ eV) but converged conduction bands ($dE = 0.04$ eV), shown in Fig. 5(a). The negative effect of increasing *dE* is clear when comparing $Mg_2Si_{0.4}Sn_{0.4}Ge_{0.2}$ to the hypothetical materials: the *PF* in $Mg_2Si_{0.4}Sn_{0.4}Ge_{0.2}$ is reduced due to the loss of band degeneracy (increased *dE*). The reduction, however, becomes less significant at high temperatures where the Fermi window, $2k_BT$, (i.e., 0.138 eV

TABLE II. Material-related parameters employed in TPB model for fitting the electrical transport properties of $Mg_2Si_{0.4}Sn_{0.6}$ samples with two different carrier concentrations.

Parameters	Literature values	Employed values
Band gap, E_g (eV)	0.61,[10] 0.54[37]	0.42[a]
Temperature coefficient of E_g, $\frac{dE_g}{dT}$ (10^{-4} eV K^{-1})	−1.6,[31] −3.28[37]	−3.5[b]
Conduction band separation, dE (eV)	0.061,[31] 0.038[32]	0.04[b]
Density-of-states effective mass of band 1, $m^*_{d,1}$ (m_0)	0.475,[31] 0.76[37]	1.5[a]
Density-of-states effective mass of band 2, $m^*_{d,2}$ (m_0)	1.2,[31] 0.98[37]	2.4[a]
Degeneracy of band 1, $N_{v,1}$	3[35]	3
Degeneracy of band 2, $N_{v,2}$	3[35]	3
Density-of-state effective mass of band 3, $m^*_{d,3}$ (m_0)	1.45[31]	1.45[b]
Mass density, ρ (g cm^{-3})	N/A	3.0[c]
Sound velocity in longitudinal direction, v_L (m s^{-1})	5400[34]	5400[b]
Number of atoms per unit volume, N_0 (m^{-3})	N/A	4.17×10^{28}[c]
Fractional alloy composition, x	0.6	0.6
Acoustic phonon deformation potential, E_{ph} (eV)	13,[34] 8.77–9.43,[35] 8.46[37]	6.73[a]
Alloy deformation potential, E_{al} (eV)	0.72,[34] 0.32–0.39[35]	0.95[a]

[a]Value extracted from measured transport properties.
[b]Value obtained from the literatures.
[c]Value calculated based on density measurement and Rietveld refinement.

at 800 K) becomes comparable to the conduction-band separation in $Mg_2Si_{0.4}Sn_{0.4}Ge_{0.2}$, $dE = 0.14$ eV. On the other hand, by comparing the calculated *PF* of the hypothetical materials to that of $Mg_2Si_{0.4}Sn_{0.6}$, it is clear that the increase of *PF* by eliminating bipolar effects (increased E_g) becomes significant at temperature above 650 K. In summary, an increased dE reduces *PF* in $Mg_2Si_{0.4}Sn_{0.6-y}Ge_y$ ($y = 0.1$ and 0.2) at low temperatures. As temperature increases, however, the effect of dE decreases and the elimination of bipolar effect becomes obvious. Finally, the calculation suggests that Ge substitution can lead to a maximum *PF* value similar to that in $Mg_2Si_{0.4}Sn_{0.6}$, while the temperature for the peak *PF* is increased.

The TPB model also enables the calculation of electronic and bipolar thermal conductivities, as shown in Fig. 5(b). The derivation details of κ_e and κ_b can be found in Appendix A. The electronic thermal conductivity is calculated by

$$\kappa_e = \kappa_{e,1} + \kappa_{e,2} + \kappa_{e,3}, \tag{4}$$

where the partial electronic thermal conductivity is related to the partial electrical conductivity of each band by the Wiedemann-Franz relationship, $\kappa_{e,i} = L_i \times \sigma_i \times T$, where L_i is the partial Lorenz number of each band. In addition, the bipolar thermal conductivity can be calculated as

$$\kappa_b = \frac{(S_1 - S_2)^2 \sigma_1 \sigma_2}{\sigma_1 + \sigma_2 + \sigma_3} T + \frac{(S_2 - S_3)^2 \sigma_2 \sigma_3}{\sigma_1 + \sigma_2 + \sigma_3} T + \frac{(S_3 - S_1)^2 \sigma_3 \sigma_1}{\sigma_1 + \sigma_2 + \sigma_3} T. \tag{5}$$

The results shown in Fig. 5(b) clearly suggest the bipolar thermal conductivity in Ge-substituted samples is effectively suppressed. The electronic contribution to the thermal conductivity in Ge-substituted samples are increased due to their higher electrical conductivity. The increase of electrical conductivity in Ge-substituted samples is owing to the improved average carrier mobility: as the conduction bands separation increases in Ge-substituted samples, more electrons are conducted in the lighter band and have higher carrier mobility since the mobility is inversely proportional to $m_b^{*5/2}$ as analyzed in Appendix B. The lattice thermal conductivity is then obtained by subtracting electronic and bipolar contributions from the total thermal conductivity. The results shown in Fig. 5(c), even when taking into account the measurement uncertainty, suggest that Ge substitutions maintain, if not further reduce, the low lattice thermal conductivity in $Mg_2Si_{0.4}Sn_{0.6}$. This trend could be intuitively understood by that Ge atoms introduce an extra degree of structure disorderness in the solid solution. Coincidentally, Kyratsi *et al.* reported low lattice thermal conductivities in Bi-doped $Mg_2Si_{0.4}Sn_{0.55}Ge_{0.05}$. They believed the introduction of Ge

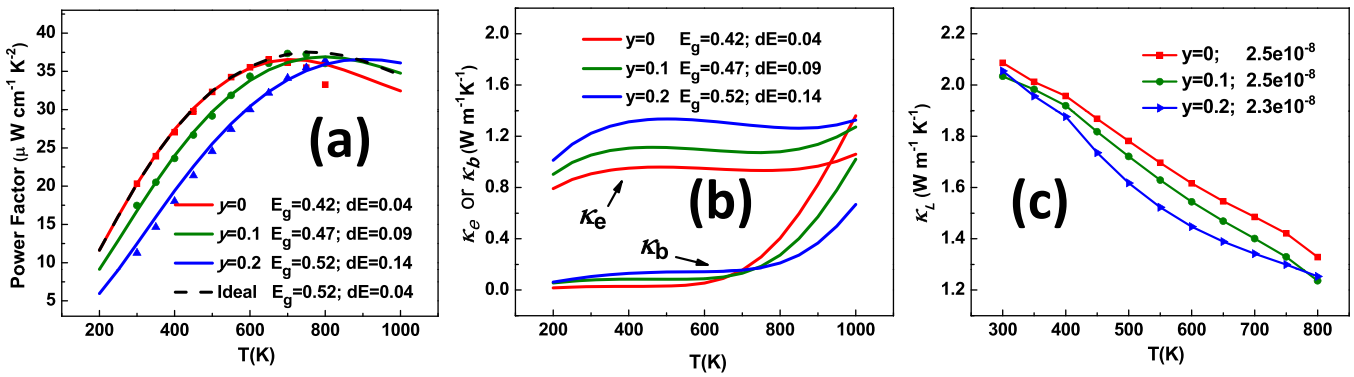

FIG. 5. (a) Temperature-dependent power factor of Sb-doped $Mg_2Si_{0.4}Sn_{0.6-y}Ge_y$ ($y = 0$, 0.1, and 0.2) with Hall coefficient of $2.4(\pm 0.2) \times 10^{-8} m^3$ C^{-1} obtained by experimental measurements (scattered symbols) and TPB-model calculation (solid lines). The black dashed curve represents the power factor of a hypothetical material with the same Hall coefficient. (b) The electronic and bipolar thermal conductivities for Sb-doped $Mg_2Si_{0.4}Sn_{0.6-y}Ge_y$ ($y = 0$, 0.1, and 0.2) with Hall coefficient of $2.4(\pm 0.2) \times 10^{-8} m^3$ C^{-1} calculated based on TPB model and (c) lattice thermal conductivities of Sb-doped $Mg_2Si_{0.4}Sn_{0.6-y}Ge_y$ ($y = 0$, 0.1, and 0.2).

increased the complexity of microstructures due to the formation of Ge-rich phase.[33] In comparison, increasing Si content in $Mg_2Si_{1-x}Sn_x$ might suppress the bipolar effects just as Ge substitution does; however, it may not simultaneously reduce the lattice thermal conductivities. In contrast, the lattice thermal conductivity of $Mg_2Si_{0.5}Sn_{0.5}$ and $Mg_2Si_{0.6}Sn_{0.4}$ were reported to be higher than that in $Mg_2Si_{0.4}Sn_{0.6}$.[11,24]

After analyzing the power factor and thermal conductivity of $Mg_2Si_{0.4}Sn_{0.6-y}Ge_y$ ($y=0$, 0.1, and 0.2), we proceed to revisit the *ZT* in $Mg_2Si_{0.4}Sn_{0.5}Ge_{0.1}$. As shown in Figs. 2(b) and 5(a), the maximum *PF* and a minimum κ of $Mg_2Si_{0.4}Sn_{0.6}$ both locate around 650 K while those of $Mg_2Si_{0.4}Sn_{0.5}Ge_{0.1}$ are found around 800 K. The peak *Z*, equals to $\frac{PF}{\kappa}$, in these two samples remain almost unchanged. Therefore, the likely small increase of *ZT* in $Mg_2Si_{0.4}Sn_{0.5}Ge_{0.1}$ at high temperatures is primarily caused by the increased peak temperature of *Z* owing to the bipolar-effect elimination.

IV. CONCLUSION

Our experimental results show that Ge substitutions in $Mg_2Si_{0.4}Sn_{0.6-y}Ge_y$ ($y=0.1$, 0.2) effectively decreased the undesirable bipolar effect presented in the parent compound $Mg_2Si_{0.4}Sn_{0.6}$. For the samples with the same Hall coefficients and thus similar carrier concentrations, the *ZT* of $Mg_2Si_{0.4}Sn_{0.5}Ge_{0.1}$ is improved slightly compared to that of $Mg_2Si_{0.4}Sn_{0.6}$ at temperatures above 650 K, although the opposite trend is found at lower temperatures. The DFT calculation suggests that Ge substitution results in not only band-gap widening, but also conduction-band splitting in $Mg_2Si_{0.4}Sn_{0.6-y}Ge_y$. The band-gap widening contributes to the elimination of bipolar conduction at high temperatures, whereas the splitting of two conduction bands is responsible for the reduced TE performance at low temperatures. To quantitatively understand these two competing effects on thermoelectric properties, we developed a triple-parabolic-band model to analyze the TE properties of $Mg_2Si_{0.4}Sn_{0.6-y}Ge_y$($y=0$, 0.1, and 0.2). The modeling results suggest that Ge substitution shifts the peak of power factor of $Mg_2Si_{0.4}Sn_{0.6-y}Ge_y$ to higher temperatures without reducing its peak value. In addition, calculation also indicates that Ge substitutions not only largely suppress the bipolar thermal conductivity but also effectively maintain, or slightly reduce, the lattice thermal conductivity of $Mg_2Si_{0.4}Sn_{0.6}$ by increasing the structure disorder.

The bipolar-effect elimination and the low lattice thermal conductivity, both induced by Ge substitution, contribute together to the slightly improved *ZT* in $Mg_2Si_{0.4}Sn_{0.5}Ge_{0.1}$ at high temperatures. Based on these findings, additional studies can be conducted to optimize the Ge substitution level to balance the trade-off of increasing E_g and dE, to optimize the carrier concentration to improve *ZT* while suppressing the bipolar effect, and to introduce other dopants or secondary phase to further reduce the lattice thermal conductivity.

Note: After the manuscript was submitted, we became aware of the work by Liu *et al.*[22] They have studied the Ge doping effects on thermoelectric properties in Mg_2Sn. Their results are consistent with the conclusions in our paper.

ACKNOWLEDGMENTS

This work was supported by National Science Foundation (NSF)-Department of Energy (DOE) Joint Thermoelectric Partnership (NSF Award No. CBET-1048767). The SPS equipment used for materials synthesis was acquired with the support of a NSF Major Research Instrumentation (MRI) award (DMR-1229131). The PPMS instrument for Hall and electrical transport measurements was acquired with the support of the NSF Materials Interdisciplinary Research Team (MIRT) award (DMR-1122603).

APPENDIX A: DERIVATION OF TRANSPORT EQUATIONS BASED ON THE TRIPLE-PARABOLIC-BAND MODEL

In the TPB model, the calculations of Seebeck coefficient (S), electrical conductivity (σ), Hall coefficient (R_H), electronic thermal conductivity (κ_e), and bipolar thermal conductivity (κ_b) consist of the contributions from three bands: the light conduction band 1 and the heavy conduction band 2 and one valence band 3. The derivation of equations described below mostly follows the two-band model in the book by Nolas *et al.*[14]

1. Electrical conductivity

The electric current density, j, consists of contributions from 3 bands

$$j = j_1 + j_2 + j_3, \tag{A1}$$

and current density in each band is driven by both external electric field and Seebeck effect

$$j_i = \sigma_i\left(-\frac{\partial\Phi}{\partial x} - S_i\frac{\partial T}{\partial x}\right), \tag{A2}$$

where Φ is the electrochemical potential, σ_i and S_i are the partial electrical conductivity and Seebeck coefficient of each band. Given the temperature gradient $\frac{\partial T}{\partial x}=0$

$$j = (\sigma_1+\sigma_2+\sigma_3)\left(-\frac{\partial\Phi}{\partial x}\right). \tag{A3}$$

Thus, Eq. (2) is obtained.

2. Seebeck coefficient

Seebeck coefficient is defined as the voltage build up under a small temperature gradient in a steady state where the electric current density $j=0$. From Eqs. (A1) and (A2)

$$(\sigma_1+\sigma_2+\sigma_3)\left(-\frac{\partial\Phi}{\partial x}\right) = (\sigma_1S_1+\sigma_2S_2+\sigma_3S_3)\left(-\frac{\partial T}{\partial x}\right). \tag{A4}$$

Thus, Eq. (1) for the Seebeck coefficient is obtained.

3. Electronic and bipolar thermal conductivity

Next, we proceed to investigate the heat flux density, w, carried by electrons or holes in 3 bands

$$w = w_1 + w_2 + w_3. \tag{A5}$$

The heat flow is driven not only by the temperature gradient but also by the Peltier effect

$$w_i = S_i T j_i - \kappa_{e,i}\frac{\partial T}{\partial x}. \tag{A6}$$

Thermal conductivity is defined in the absence of electric current, i.e., $j = 0$, which keeps Eqs. (A4) and (1) valid. This allows us to rearrange Eq. (A2) as follows:

$$j_i = \sigma_i(S - S_i)\frac{\partial T}{\partial x}. \tag{A7}$$

By plugging Eqs. (A6) and (A7) into (A5), we obtained

$$\begin{aligned} w = &-(\kappa_{e,1} + \kappa_{e,2} + \kappa_{e,3})\frac{\partial T}{\partial x} + T[(S_1\sigma_1(S - S_1) \\ &+ (S_2\sigma_2(S - S_2) + (S_3\sigma_3(S - S_3)]\frac{\partial T}{\partial x}. \end{aligned} \tag{A8}$$

After inserting Eq. (1) into the second part of Eq. (A8), we obtained

$$\begin{aligned} w = &-(\kappa_{e,1} + \kappa_{e,2} + \kappa_{e,3})\frac{\partial T}{\partial x} - \left[\frac{(S_1 - S_2)^2\sigma_1\sigma_2}{\sigma_1 + \sigma_2 + \sigma_3}T \right. \\ &\left. + \frac{(S_2 - S_3)^2\sigma_2\sigma_3}{\sigma_1 + \sigma_2 + \sigma_3}T + \frac{(S_3 - S_1)^2\sigma_3\sigma_1}{\sigma_1 + \sigma_2 + \sigma_3}T\right]\frac{\partial T}{\partial x}. \end{aligned} \tag{A9}$$

Therefore, the total thermal conductivity contributed by charge carriers is

$$\begin{aligned} \kappa_{e,tot} = &(\kappa_{e,1} + \kappa_{e,2} + \kappa_{e,3}) + \left[\frac{(S_1 - S_2)^2\sigma_1\sigma_2}{\sigma_1 + \sigma_2 + \sigma_3}T \right. \\ &\left. + \frac{(S_2 - S_3)^2\sigma_2\sigma_3}{\sigma_1 + \sigma_2 + \sigma_3}T + \frac{(S_3 - S_1)^2\sigma_3\sigma_1}{\sigma_1 + \sigma_2 + \sigma_3}T\right], \end{aligned} \tag{A10}$$

where the first part of Eq. (A10), as shown in Eq. (4), is the sum of the partial electronic thermal conductivity of each band. This part is sometimes called the electronic thermal conductivity. It is important to distinguish this part from the total electronic thermal conductivity $\kappa_{e,tot}$. The second part of Eq. (A10), as shown in Eq. (5), is the sum of the thermal conductivity originated from the Peltier effect interacting between bands. This is the so-called bipolar thermal conductivity.

4. Hall coefficient

To derive the Hall coefficient for the TPB model, we first assign the Hall carrier concentration in each band to be n_1, n_2, and n_3. Here, n_1, n_2 are the electron concentration and n_3 is the hole concentration. The Hall measurement is carried out on a rectangular sample with the presence of a magnetic field (B_z) perpendicular to the sample. The current at x direction (J_x) and the voltage (E_y) at y direction are measured while the current at y direction (J_y) is zero. J_y consists of the contributions of three bands

$$J_y = en_1v_{1,y} + en_2v_{2,y} + en_3v_{3,y} = 0, \tag{A11}$$

where $v_{1,y}$ ($i = 1, 2, 3$) is the drift velocity at y direction of carriers in band i. The carriers are driven by not only the electrostatic force, but also the Lorentz force: $v_{i,y} = \mu_i(E_y + v_{i,x}B_z)$. Thus, Eq. (A11) can be rearranged as

$$\begin{aligned} &E_y(n_1\mu_1 + n_2\mu_2 + n_3\mu_3) \\ &\quad = B_zE_x(-n_1{\mu_1}^2 - n_2{\mu_2}^2 + n_3{\mu_3}^2). \end{aligned} \tag{A12}$$

The current in the x direction can be expressed as $J_x = en_1v_{1,x} + en_2v_{2,x} + en_3v_{3,x}$. Since there is no net current in the y direction, J_x is free of the Lorentz term. Thus, $J_x = eE_x(n_1\mu_1 + n_2\mu_2 + n_3\mu_3)$. By replacing E_x in Eq. (A12) with J_x, we thus obtain the expression of R_H for the TPB model

$$\begin{aligned} R_H &= (E_y/J_x)/B_z \\ &= \frac{-n_1{\mu_1}^2 - n_2{\mu_2}^2 + n_3{\mu_3}^2}{e(n_1\mu_1 + n_2\mu_2 + n_3\mu_3)^2}. \end{aligned} \tag{A13}$$

For each band i, the partial electrical conductivity and Hall coefficient are $\sigma_i = en_i\mu_i$ and $R_{H,i} = \pm 1/en_i$. Thus, Eq. (A13) can be expressed by the partial Hall coefficient of each band, as presented in Eq. (3). It should be pointed out that n_i and μ_i employed in this derivation of R_H are actually the Hall carrier concentration $n_{H,i}$ and Hall mobility $\mu_{H,i}$, respectively. The subscript H was previously neglected for simplicity. The relationship between Hall carrier concentration and actual carrier concentration is $n_{H,i} = \frac{n_i}{r_{H,i}}$, between Hall mobility and actually mobility is $\mu_{H,i} = \mu_i r_{H,i}$. Here, $r_{H,i}$ is the Hall factor of band i, the detailed equation of which will be introduced Appendix B.

APPENDIX B: EQUATIONS OF PARTIAL TRANSPORT PROPERTIES OF EACH BAND

As derived in Appendix A, Seebeck coefficient (S), electrical conductivity (σ), and Hall coefficient (R_H) can be calculated based on the partial transport properties S_i, σ_i, and $R_{H,i}$ of each band. Here, we list the equations for these partial transport properties as follows.

The partial Seebeck coefficient contribution from band i is represented as

$$S_i = \frac{k_B}{e}\left[\frac{\left(r + \frac{5}{2}\right)F_{\frac{3}{2}+r}(\xi_i)}{\left(r + \frac{3}{2}\right)F_{\frac{1}{2}+r}(\xi_i)} - \xi_i\right], \tag{B1}$$

where k_B is the Boltzmann constant, e is the elemental charge, and $\xi_i = \frac{E_f - E_i}{k_BT}$ is the reduced Fermi level for band i with the band edge located at E_i. In this TPB model, $\xi_1 = \frac{E_f - E_1}{k_BT}$, $\xi_2 = \xi_1 - \frac{dE}{k_BT}$ and $\xi_3 = -\xi_1 - \frac{E_g}{k_BT}$. r is the scattering

parameter, which takes the value of −0.5 for both alloy scattering and acoustic phonon scattering mechanisms[14] presented in $Mg_2Si_xSn_{1-x}$ solid solutions.[34,35] The partial electrical conductivity and Hall coefficients are given as

$$\sigma_i = n_i e \mu_i \tag{B2}$$

and

$$R_{H,i} = \frac{r_{H,i}}{n_i e}, \tag{B3}$$

respectively, where n_i is the carrier concentration conducted in each band ($i = 1$, 2, and 3)

$$n_i = \frac{1}{2\pi^2\hbar^3}(2k_BT)^{\frac{3}{2}} m_{d,i}^{*\frac{3}{2}} F_{\frac{1}{2}}(\xi_i), \tag{B4}$$

and $r_{H,i}$ is the Hall factor in band i and given as

$$r_{H,i} = \frac{3}{2}\frac{\left(2r+\frac{3}{2}\right)}{\left(r+\frac{3}{2}\right)^2}\frac{F_{\frac{1}{2}}(\xi_i)F_{\frac{1}{2}+2r}(\xi_i)}{2F_{r+\frac{1}{2}}{}^2(\xi_i)}. \tag{B5}$$

In the above equations, $F_n(\xi_i)$ is the Fermi-Dirac integral

$$F_n(\xi_i) = \int_0^\infty \frac{x^n}{1+e^{x-\xi_i}}\,dx, \tag{B6}$$

$m_{d,i}^*$ is the density-of-states effective mass of band i and μ_i is the drift mobility of charge carriers in band i. In $Mg_2Si_xSn_{1-x}$ solid solutions, we should take into account two primary carrier scattering mechanisms including alloy scattering and acoustic phonon scattering.[34,35] Thus, μ_i is obtained from the Matthiessen's rule

$$\frac{1}{\mu_i} = \frac{1}{\mu_{al,i}} + \frac{1}{\mu_{ph,i}}, \tag{B7}$$

where $\mu_{al,i}$ is the carrier mobility resulting from pure alloy scattering[34]

$$\mu_{al,i} = \frac{16e\hbar^4}{9\sqrt{2}\pi x(1-x)(k_BT)^{\frac{1}{2}}}\frac{N_0}{E_{al}{}^2 m_{b,i}^{*\frac{3}{2}} m_{l,i}^*}\frac{F_0(\xi_i)}{F_{\frac{1}{2}}(\xi_i)}, \tag{B8}$$

and $\mu_{ph,i}$ is the carrier mobility resulting from acoustic phonon scattering[34]

$$\mu_{ph,i} = \frac{\sqrt{2}\pi e\hbar^4}{3(k_BT)^{\frac{3}{2}}}\frac{v_L{}^2\rho}{E_{ph}{}^2 m_{b,i}^{*\frac{3}{2}} m_{l,i}^*}\frac{F_0(\xi_i)}{F_{\frac{1}{2}}(\xi_i)}. \tag{B9}$$

Here, $\hbar$, x, N_0, v_L, and ρ are the reduced Planck constant, the fractional alloy composition, number of atoms per unit volume, longitudinal sound velocity, and sample density, respectively. E_{al} and E_{ph} is the alloy and acoustic phonon deformation potential constant, respectively. In addition, $m_{b,i}{}^*$ is the single valley density-of-states effective mass of band i, related to $m_{d,i}{}^*$ by $m_{d,i}{}^* = N_{v,i}{}^{\frac{2}{3}} m_{b,i}{}^*$. $N_{v,i}$ is the valley degeneracy of band i. $m_{l,i}{}^*$ is the inertia effective mass of the valley, which relates carrier mobility μ to its relaxation time τ. In Mg_2(Si, Sn, and Ge) solid solutions, the constant energy surface of conduction band is ellipsoidal because their band edges locate at the X point of the Brillouin zone. In this case, $m_{l,i}{}^*$ is not equivalent but proportional to $m_{b,i}{}^*$ by $\frac{m_{b,i}{}^*}{m_{l,i}{}^*} = \left(\frac{1}{K}\right)^{\frac{2}{3}}\frac{(2K+1)}{3}$,[36] where K is the ratio of longitudinal (m_l) to transverse (m_t) effective mass of the ellipsoidal constant energy surface. Thus, the carrier mobility μ is proportional to $m_b{}^{*-\frac{5}{2}}$ of the conducting band.

As mentioned earlier, the partial electronic thermal conductivity is related to the partial electrical conductivity by the Wiedemann-Franz relationship, $\kappa_{e,i} = L_i \times \sigma_i \times T$, where Li is the partial Lorenz number

$$L_i = \left(\frac{k_B}{e}\right)^2\left[\frac{\left(r+\frac{7}{2}\right)F_{r+\frac{5}{2}}(\xi_i)}{\left(r+\frac{3}{2}\right)F_{r+\frac{3}{2}}(\xi_i)} - \left[\frac{\left(r+\frac{7}{2}\right)F_{r+\frac{5}{2}}(\xi_i)}{\left(r+\frac{3}{2}\right)F_{r+\frac{3}{2}}(\xi_i)}\right]^2\right]. \tag{B10}$$

APPENDIX C: FIT PARAMETERS OF ELECTRICAL TRANSPORT PROPERTIES OF $Mg_2Si_{0.4}Sn_{0.6}$

By fitting the measured transport properties of the two $Mg_2Si_{0.4}Sn_{0.6}$ samples with different carrier concentrations, we obtained some of the fundamental parameters, as listed in Table II.

1. Calculation of $m_1{}^*$, $m_2{}^*$, $n_{1,300K} + n_{2,300K}$

First of all, we obtained density-of-states effective masses of two conduction bands ($m_1{}^*$ and $m_2{}^*$) and activated dopant concentrations ($n_d{}^+$) from S, σ, and R_H results measured at room temperature, where the contribution of valence band 3 is negligible. For the two $Mg_2Si_{0.4}Sn_{0.6}$ samples with different Hall coefficients of a and b, their S, σ, and R_H are functions of ($m_{1,a}{}^*$, $m_{2,a}{}^*$, $\mu_{1,a}$, $\mu_{2,a}$, $\xi_{1,a}$, $\xi_{2,a}$) and ($m_{1,b}{}^*$, $m_{2,b}{}^*$, $\mu_{1,b}$, $\mu_{2,b}$, $\xi_{1,b}$, $\xi_{2,b}$), respectively. We assume that the bottoms of each conduction bands are parabolic so that density-of-states effective masses remain the same where the Fermi level changes slightly inside the band bottom. With this assumption, $m_{1,a}{}^* = m_{1,b}{}^* = m_1{}^*$ and $m_{2,a}{}^* = m_{2,b}{}^* = m_2{}^*$. Meanwhile, ξ_2 is related to ξ_1 by $\xi_2 = \xi_1 - \frac{dE}{k_BT}$ where $dE = 0.04$ eV for $Mg_2Si_{0.4}Sn_{0.6}$; and μ_2 is related to μ_1 by $\mu_2 = \mu_1\left(\frac{m_1^*}{m_2^*}\right)^{\frac{5}{2}}$ where their band degeneracy are the same. Up to this point, all six measured parameters, S_a, σ_a, $R_{H,a}$, S_b, σ_b, and $R_{H,b}$, are the functions of six variables, namely, $m_1{}^*$, $m_2{}^*$, $\mu_{1,a}$, $\mu_{1,b}$, $\xi_{1,a}$, and $\xi_{1,b}$. We were thus able to numerically extract the values of $m_1{}^*$, $m_2{}^*$, $\mu_{1,a}$, $\mu_{1,b}$, $\xi_{1,a}$, and $\xi_{1,b}$ from these 6 equations. With the obtained $m_1{}^*$, $m_2{}^*$, and ξ_1, we can calculate the electron concentration at 300 K, $n_{1,300K} + n_{2,300K}$ by Eq. (B4).

2. Calculation of temperature-dependent reduced Fermi level $\xi_{i,T}$

Next we calculated the temperature-dependent reduced Fermi level ($\xi_{i,T}$) from the charge neutrality equation. As temperature increases, the intrinsic electrons from valence

band 3 are thermally excited to band 1 and 2, which also creates holes in valence band 3. Thus, the charge neutrality equation is expressed as $n_{1,T} + n_{2,T} = n_d{}^+ + n_{3,T}$, where $n_d{}^+$ is the activated dopant concentration. With the assumption that all dopants have been activated at room temperature, $n_d{}^+$ is equal to the electron concentration at 300 K, $n_{1,300K} + n_{2,300K}$, which was calculated above. At any specific temperature T, $n_{i,T}$ is the function of $m_i{}^*$ and $\xi_{i,T}$. We adopted the value of $m_1{}^*$ and $m_2{}^*$ obtained earlier and $m_3{}^*$ from the literature.[31] Meanwhile, $\xi_{2,T}$ and $\xi_{3,T}$ are related to $\xi_{1,T}$ by $\xi_{2,T} = \xi_{1,T} - \frac{dE}{k_B T}$ and $\xi_{3,T} = -\xi_{1,T} - \frac{E_g{}^T}{k_B T}$ where $E_g{}^T = E_g{}^0 + \beta \times T$. dE is the conduction band separation energy, E_g^0 is the band gap at 0 K, and β is the temperature dependence of the band gap. We adopted $dE = 0.04$ eV and the value of β, -3.5×10^{-4} eV/K, from the literature.[32,37] Thus, with any given E_g^0, $\xi_{1,T}$ became the only variable in the charge neutrality equation and could be numerically calculated at any specific temperature.

3. Fit band gap E_g^0 and deformation potential constants E_{ph} and E_{al}

By pre-defining a value of E_g^0, we could calculate the temperature-dependent $\xi_{1,T}$ and the temperature-dependent Seebeck coefficient by plugging the as-obtained $\xi_{1,T}$ into Eqs. (B1) and (1). By plugging Eq. (B4) and the relationship $\mu_i \propto m_{b,i}^{*\,-\frac{5}{2}} \frac{F_0(\xi_i)}{F_{\frac{1}{2}}(\xi_i)}$ into Eq. (B2), we derive that at any specific temperature, partial electrical conductivity σ_i is proportional to $\frac{N_{v,i}}{m_{b,i}^*} F_0(\xi_i)$. Combining this derived result with Eqs. (B1) and (1), it is clear that the value of Seebeck coefficient only depends on 3 sets of variables: reduced Fermi level $\xi_{i,T}$, band degeneracy $N_{v,i}$, and effective mass $m_{b,i}^*$ of each band. With known $m_{b,i}^*$ and $N_{v,i}$, the only variables are the E_g^0-associated $\xi_{i,T}$. By fitting the temperature-dependence of Seebeck coefficient, we thus obtained the self-consistent band gap $E_g^0 = 0.42$ eV of $Mg_2Si_{0.4}Sn_{0.6}$.

Subsequently, we calculated the temperature-dependent electrical conductivity and then extracted the two deformation potential constants E_{ph} and E_{al} by fitting the temperature-dependence of electrical conductivity. Since the ratio between $m_{b,i}^*$ and $m_{l,i}^*$ is unknown, we took it to be unity. This shall not affect the fitting and calculation because the actual ratio would be absorbed into the deformation potential constants, E_{ph} and E_{al}. However, for the purpose of calculating the accurate deformation energy potential constants, future effort should be made to define the accurate $\frac{m_{b,i}^*}{m_{l,i}^*}$ ratio. Both the fitted and experimental Seebeck coefficient and electrical conductivity of $Mg_2Si_{0.4}Sn_{0.6}$ are shown in Fig. 6(a).

APPENDIX D: CALCULATION OF TRANSPORT PROPERTIES OF $Mg_2Si_{0.4}Sn_{0.5}Ge_{0.1}$ AND $Mg_2Si_{0.4}Sn_{0.4}Ge_{0.2}$

With parameters obtained by fitting the electrical properties of $Mg_2Si_{0.4}Sn_{0.6}$, now we proceed to calculate the transport properties of Ge-substituted samples. The small conduction band separation (dE) in $Mg_2Si_xSn_{1-x}$ solid solution has been believed to be the key factor to its high TE performance. On the other hand, the bipolar effect resulted from the small band gap (E_g) could significantly suppress the TE properties at high temperatures. Therefore, we altered only these most important parameters, the band gap (E_g^0) and the conduction-band separation (dE) while assuming other modeling parameters remain similar as in $Mg_2Si_{0.4}Sn_{0.6}$.

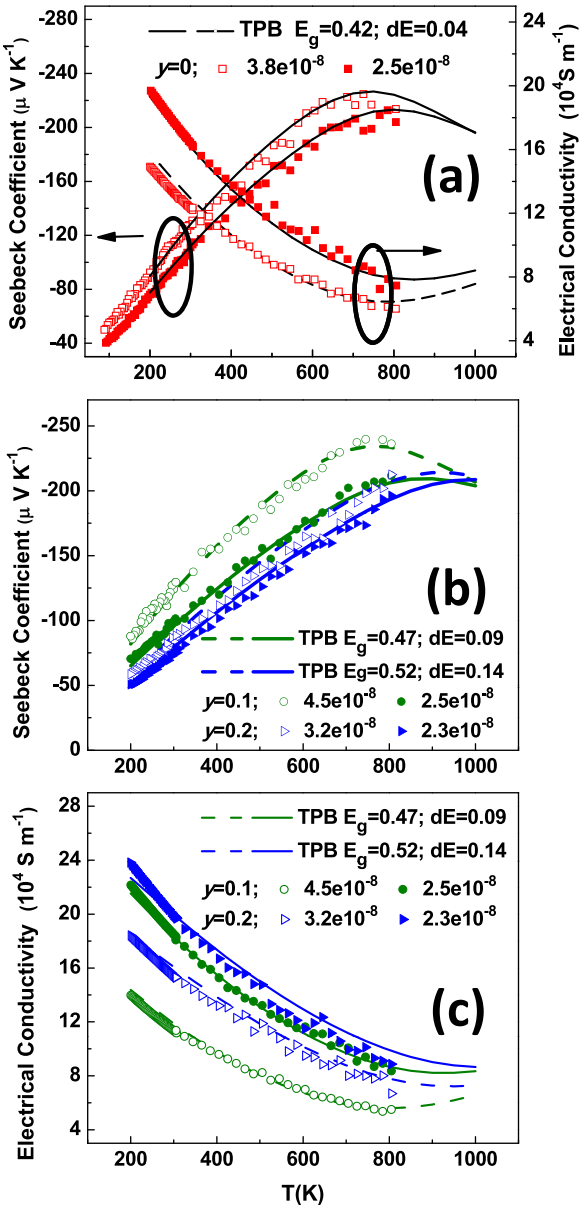

FIG. 6. (a) Fitted temperature dependence of Seebeck coefficient and electrical conductivity of two $Mg_2Si_{0.4}Sn_{0.6}$ samples with two different carrier concentrations, with comparison to the experimental results; (b) and (c) temperature dependences of Seebeck coefficient and electrical conductivity of $Mg_2Si_{0.4}Sn_{0.5}Ge_{0.1}$ and $Mg_2Si_{0.4}Sn_{0.4}Ge_{0.2}$ samples calculated by TPB model with comparison to experimental results. The lines represent calculation results, while the symbols are experimental data. The dashed lines (hollow symbols) represent the samples with high Hall coefficients, while the solid lines (filled symbols) represent the samples with low Hall coefficients.

1. Calculation of activated dopant concentration from room-temperature R_H

The extrinsic electron concentrations $n_{1,300K} + n_{2,300K}$ were calculated based on room-temperature R_H results. From Eqs. (B3) and (3), combined with previous derivation,

$\sigma_i \propto \frac{N_{v,i}}{m^*_{b,i}} F_0(\xi_i)$, it is clear that the R_H is a function of $N_{v,i}$, $m^*_{b,i}$, and ξ_i $(i=1,2)$. With known $N_{v,i}$ and $m^*_{b,i}$ and the relationship between $\xi_{2,300K}$ and $\xi_{1,300K}$, i.e., $\xi_{2,300K} = \xi_{1,300K} - \frac{dE}{k_B T}$, it is straightforward to calculate $\xi_{1,300K}$ and thus $n_{1,300K} + n_{2,300K}$ from the room-temperature R_H results.

2. Calculation of temperature-dependent $\xi_{1,T}$ from the charge neutrality equation

As temperature increases, the temperature-dependent reduced Fermi level $\xi_{1,T}$ was obtained from the charge neutrality equation with known extrinsic carrier concentration $n_{1,300K} + n_{2,300K}$, similar to the procedure we described in $Mg_2Si_{0.4}Sn_{0.6}$ case. With known $\xi_{1,T}$, E_g, and dE, $\xi_{2,T}$ and $\xi_{3,T}$ can be calculated.

3. Calculation of temperature-dependent *S* and σ

By applying $\xi_{i,T}$ $(i=1, 2, 3)$ into related equations, we thus calculated the temperature-dependent partial transport properties, S_i and σ_i $(i=1, 2, 3)$. The total S and σ were calculated by using Eqs. (1) and (2). As shown in Figs. 6(b) and 6(c), the calculated S and σ results agreed well with experimental data.

APPENDIX E: CALCULATION OF TEMPERATURE-DEPENDENT κ_e AND κ_b OF $Mg_2Si_{0.4}Sn_{0.6-y}Ge_y$ ($y = 0$, 0.1, and 0.2)

By plugging $\xi_{i,T}$ $(i=1, 2, 3)$ into related equations, we obtained L_i, σ_i, and thus κ_e by using Eq. (4). By plugging S_i and σ_i $(i=1, 2, 3)$ into Eq. (5), we then calculated the κ_b.

[1]Y. Pei, X. Shi, A. LaLonde, H. Wang, L. Chen, and G. J. Snyder, Nature **473**, 66 (2011).
[2]J. P. Heremans, V. Jovovic, E. S. Toberer, A. Saramat, K. Kurosaki, A. Charoenphakdee, S. Yamanaka, and G. J. Snyder, Science **321**, 554 (2008).
[3]L.-D. Zhao, S.-H. Lo, Y. Zhang, H. Sun, G. Tan, C. Uher, C. Wolverton, V. P. Dravid, and M. G. Kanatzidis, Nature **508**, 373 (2014).
[4]G. J. Snyder and E. S. Toberer, Nat. Mater. **7**, 105 (2008).
[5]G. Nolas, J. Cohn, G. Slack, and S. Schujman, Appl. Phys. Lett. **73**, 178 (1998).
[6]B. Sales, D. Mandrus, and R. K. Williams, Science **272**, 1325 (1996).
[7]X. Wang, H. Lee, Y. Lan, G. Zhu, G. Joshi, D. Wang, J. Yang, A. Muto, M. Tang, J. Klatsky *et al.*, Appl. Phys. Lett. **93**, 193121 (2008).
[8]B. Poudel, Q. Hao, Y. Ma, Y. Lan, A. Minnich, B. Yu, X. Yan, D. Wang, A. Muto, D. Vashaee *et al.*, Science **320**, 634 (2008).
[9]K. Biswas, J. He, Q. Zhang, G. Wang, C. Uher, V. P. Dravid, and M. G. Kanatzidis, Nat. Chem. **3**, 160 (2011).
[10]V. Zaitsev, M. Fedorov, E. Gurieva, I. Eremin, P. Konstantinov, A. Y. Samunin, and M. Vedernikov, Phys. Rev. B **74**, 045207 (2006).
[11]W. Liu, X. Tan, K. Yin, H. Liu, X. Tang, J. Shi, Q. Zhang, and C. Uher, Phys. Rev. Lett. **108**, 166601 (2012).
[12]V. Zaitsev, M. Fedorov, I. Eremin, and E. Gurieva, *Thermoelectrics Handbook: Macro to Nano* (CRC Press, 2005).
[13]P. Price, Philos. Mag. **46**, 1252 (1955).
[14]G. S. Nolas, J. Sharp, and H. J. Goldsmid, *Thermoelectrics: Basic Principles and New Materials Developments* (Springer, 2001), Vol. 45.
[15]T. M. Tritt and M. Subramanian, MRS Bull. **31**, 188 (2006).
[16]Y. Pei, H. Wang, and G. Snyder, Adv. Mater. **24**, 6125 (2012).
[17]M. Fedorov, E. Gurieva, I. Eremin, P. Konstantinov, A. Y. Samunin, V. Zaitsev, S. Sano, and L. Rauscher, in *Proceedings of the 2nd European Conference on Thermoelectrics* (2004), pp. 72–74.
[18]K. Kutorasinski, J. Tobola, S. Kaprzyk, A. Khan, and T. Kyratsi, J. Electron. Mater. **43**, 3831 (2014).
[19]A. Khan, N. Vlachos, E. Hatzikraniotis, G. Polymeris, C. B. Lioutas, E. Stefanaki, K. Paraskevopoulos, I. Giapintzakis, and T. Kyratsi, Acta Mater. **77**, 43 (2014).
[20]L. Zhang, L. Shi, J. B. Goodenough, and J. Zhou, "ALD alumina oxide as protective coating against degradation of $Mg_2Si_{1-x}Sn_x$ compounds upon heat treatment" (unpublished).
[21]W. Liu, X. Tang, H. Li, J. Sharp, X. Zhou, and C. Uher, Chem. Mater. **23**, 5256 (2011).
[22]J.-W. Liu, M. Song, M. Takeguchi, N. Tsujii, and Y. Isoda, J. Electron. Mater. **44**, 407 (2015).
[23]Q. Zhang, J. He, T. Zhu, S. Zhang, X. Zhao, and T. Tritt, Appl. Phys. Lett. **93**, 102109 (2008).
[24]W. Liu, X. Tang, H. Li, K. Yin, J. Sharp, X. Zhou, and C. Uher, J. Mater. Chem. **22**, 13653 (2012).
[25]J. Heyd, G. E. Scuseria, and M. Ernzerhof, J. Chem. Phys. **118**, 8207 (2003).
[26]J. Heyd and G. E. Scuseria, J. Chem. Phys. **121**, 1187 (2004).
[27]J. Heyd, G. E. Scuseria, and M. Ernzerhof, J. Chem. Phys. **124**, 219906 (2006).
[28]P. E. Blöchl, Phys. Rev. B **50**, 17953 (1994).
[29]G. Kresse and D. Joubert, Phys. Rev. B **59**, 1758 (1999).
[30]J. Pulikkotil, D. Singh, S. Auluck, M. Saravanan, D. Misra, A. Dhar, and R. Budhani, Phys. Rev. B **86**, 155204 (2012).
[31]M. Fedorov, D. Pshenay-Severin, V. Zaitsev, S. Sano, and M. Vedernikov, in *22nd International Conference on Thermoelectrics (ICT)* (IEEE, 2003), pp. 142–145.
[32]X. Tan, W. Liu, H. Liu, J. Shi, X. Tang, and C. Uher, Phys. Rev. B **85**, 205212 (2012).
[33]G. Polymeris, N. Vlachos, A. Khan, E. Hatzikraniotis, C. B. Lioutas, A. Delimitis, E. Pavlidou, K. Paraskevopoulos, and T. Kyratsi, Acta Mater. **83**, 285 (2015).
[34]X. Liu, T. Zhu, H. Wang, L. Hu, H. Xie, G. Jiang, G. J. Snyder, and X. Zhao, Adv. Energy Mater. **3**, 1238 (2013).
[35]W. Liu, H. Chi, H. Sun, Q. Zhang, K. Yin, X. Tang, Q. Zhang, and C. Uher, Phys. Chem. Chem. Phys. **16**, 6893 (2014).
[36]V. Zaitsev, M. Fedorov, A. Burkov, E. Gurieva, I. Eremin, P. Konstantinov, S. Ordin, S. Sano, and M. Vedernikov, in *21st International Conference on Thermoelectrics (ICT'02)* (IEEE, 2002), pp. 151–154.
[37]J.-H. Bahk, Z. Bian, and A. Shakouri, Phys. Rev. B **89**, 075204 (2014).